Indonesian Journal of Physics and Nuclear Applications
Volume 4, Number 2, June 2019, p. 45-57
e-ISSN 2550-0570, © FSM UKSW Publication

MEASUREMENT OF YTTRIUM-90 BIODISTRIBUTION IN SELECTIVE INTERNAL RADIATION THERAPY (SIRT): A COMPARISON BETWEEN PET AND SPECT IMAGING

Sita Gandes Pinasti[1*]
[1]*Medical Radiation Physics/Radiation Protection, Medical Faculty Mannheim, Heidelberg University*
Theodor-Kutzer-Ufer, 68167 Mannheim, Germany

ARTICLE INFO

Article history:

Received: 14 August 2018
Received in revised form: 04 September 2019
Accepted: 30 September 2019

Keywords:

Post-radioembolization imaging
90Y
PET
SPECT
Biodistribution measurements

A B S T R A C T

Measurement of radionuclides biodistribution in post-radioembolization 90Y SIRT is a part of treatment evaluation, in which the assessment of biodistribution is used to evaluate the possible extrahepatic presence and the absorbed dose estimation for the tumor cells, healthy liver cells, and critical organs. As the dose-response analysis is performed based on this evaluation, the biodistribution measurement coming from post-imaging modality has a crucial role in achieving these goals. The two devices, Single Photon Emission Tomography (SPECT) and Positron Emission Tomography are discussed in some aspects, including the quality of quantitative images, performance characteristics, and absorbed dose considerations.

1. INTRODUCTION

Radioembolization by Selective Internal Radiation Therapy (SIRT) using ^{90}Y is a preferable treatment option for inoperable primary liver malignancy and colorectal metastases in the liver (Murthy et al., 2005). In these malignancies, external radiotherapy is not favorable due to liver cell intolerance and complications (such as hepatitis and progressive liver failure) after 30 Gy dose for liver (Stubbs & Wickremesekera, 2004). Yttrium-90 is a beta emitter with high energy ($E_{\beta mean}$=0.94 MeV) which can deliver a significant amount of dose (up to 80 Gy) and thus increase treatment efficacy (Pasciak, Bradley, & McKinney, 2017). The ^{90}Y radionuclide along with its carrier substance is provided through catheters directly to the intrahepatic artery. The carrier element can be either in the form of resin or glass microsphere; each has its particular application. Resin microsphere is aimed for primary colorectal cancer while glass microsphere is aimed for unresectable primary liver cancer (Giammarile et al., 2011). Since the liver is surrounded by many critical soft tissues and organs, a careful treatment planning is required to minimize potential complications. It was reported that extrahepatic accumulation of ^{90}Y could lead to several side effects, such as ulceration, bleeding of the gastrointestinal track, and radiation pneumonitis (Leung TW, 1995; Murthy et al., 2007; Riaz et al., 2009). Due to the nature of malignant cells, in which they require more blood supply compared to the normal cell, there is a unique process which can be used as a basis for malignant treatment based on SIRT. The distinct character of malignant hepatic cells is that they obtain their blood supply mainly from the hepatic artery, while the normal hepatic cells get their blood supply from the portal vein (Biermann HR, 1951). Based on

* Corresponding author. Tel.: +62 8995139341; E-mail address: sita.gandes.p@gmail.com

this fact, a radioembolization method can be employed to target the malignant cells selectively.

The procedure of radioembolization includes the restriction of arterial bifurcation connecting the malignant site to the adjacent organs (Lau et al., 2012). In doing so, first, vascular mapping and radioembolization processes are done by using a microcatheter guided by fluoroscopy. Second, to estimate the potential spreading of the radionuclide to the lung, an assessment of lung shunting fraction (LSF) by using a surrogate radiopharmaceutical (^{99}Tc-MAA) is performed by using gamma camera for adjusting the activity administered to be given to the patient. There is a guideline from the manufacturer for each type of microsphere. For resin microspheres, there is no reduction of administered activity for LSF<10%, 20% reduction of 10-15% LSF, 40% reduction for 15-20% LSF, and no treatment if the amount of LSF found to be higher than 20% (SIR-Spheres®, Sirtex Medical, Lane Cove, Australia). For glass microspheres, there is no such reduction factor, but the activity is limited by the amount of lung dose, i.e. <30 Gy for a single treatment and <50 Gy for cumulative treatment (TeraSphere®, MDS Nordion, Canada). The third step is activity planning. There are several methods available, namely, the body surface area (BSA) method (Kao YH, 2011), the partition model (PM) (Ho S, 1997), and medical internal radiation dosimetry (MIRD) (Gulec, Mesoloras, & Stabin, 2006; Stabin, 2006) for the resin microspheres. Whereas, for glass microsphere, the compartmental MIRD microdosimetry (Doherty, 2015) is used. Once the amount of activity has been decided, the ^{90}Y microsphere is infused into the hepatic artery by microcatheter guided by fluoroscopy (Lau et al., 2012). Following these steps, the treatment evaluation is performed after one day for the sake of three purposes. First, to assess the extrahepatic transfer of the radionuclide, second, to know the prognosis for the response of the lesion, and the last, to estimate absorbed dose obtained by both the cancerous and normal liver sites as well as the critical organs (Giammarile et al., 2011).

A general formalism of the Medical Internal Radiation Dosimetry (MIRD) developed by the Society of Nuclear Medicine (SNM) takes into account several parameters, including the biodistribution of the radionuclide and the contributing physical factor, which are specified as time-integrated activity and S-value (Stabin, 2008). Nowadays, the measurement of biodistribution uses a quantitative imaging approach which can provide a more accurate yet non-invasive procedure. Our particular concern in this review was to discuss the available tools for measuring biodistribution of activity in the post-treatment of ^{90}Y SIRT based on quantitative imaging. The scope of the review was intentionally restricted only to Positron Emission Tomography (PET) and Single Photon Emission Tomography (SPECT) as these are the primary modalities which can quantify biodistribution of activity of ^{90}Y microspheres in multiple views, which cannot be obtained in planar imaging, such as the gamma camera. It is of our interest because the biodistribution of activity can affect absorbed dose accuracy estimation and will guide the assessment of treatment efficacy, the decision for additional dose for the patient, and dose-response analyses (Stabin, 2008).

2. MATERIALS AND METHODS

2.1 Current Techniques For 90y Imaging

Yttrium-90 is a common therapeutic radionuclide which can be produced via ^{89}Y(n,γ)^{90}Y reaction in a nuclear reactor, or via the ^{90}Sr decay. Figure 1 shows the decay of ^{90}Y to ^{90}Zr which emits beta particles as the major decay scheme. It has a half-life of 2.6684 days, beta energy of 2.28 MeV (max) and 0.937 MeV (mean), tissue penetration depth of 11 mm (max) and 2.5 mm (mean) which make it suitable to irradiate the size of either metastatic or primary tumor in the liver (Bé, 2006). Also, the ^{90}Y decays completely within 13 days, a desirable characteristic that provides the maximum balance between treatment time and

patient safety.

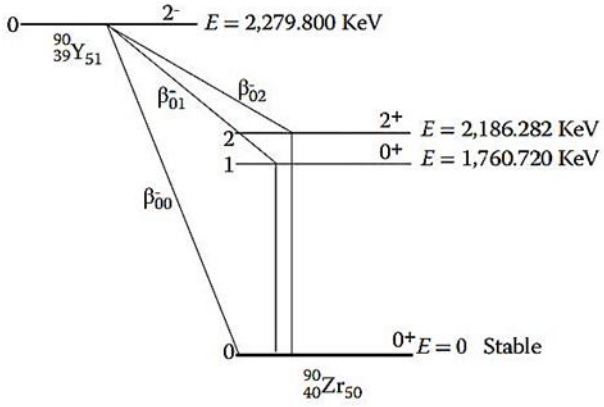

Fig 1. The decay scheme of ^{90}Y to ^{90}Zr. Although the majority of ^{90}Y decays via β- emission, there is a small portion of decay via the excitation state of 90Zr (E=1.76 keV) with branching ratio of $(3.186\pm0.047)\times10^{-5}$. The picture was reproduced based on Selwyn, Nickles, Thomadsen, DeWerd, & Micka, 2007.

At the beginning of the use of radioembolization ^{90}Y SIRT, there was common knowledge that ^{90}Y was a pure β^- emitter and that was the reason why SPECT is the only choice to measure the biodistribution of ^{90}Y through the bremsstrahlung photons produced by the interaction between β^- and tissue (Bailey & Willowson, 2013). Though people realized that the image quality is relatively poor for quantitative measurement, SPECT was still extensively used for post-treatment evaluation as no other option was available. Despite the fact that Ford had predicted the 0^+–0^- transition of ^{90}Zr producing β^+ and been experimentally discovered by Johnson, et al. in 1955 (Ford, 1955; Johnson O, 1955), it still needs a long way to go until the PET-based quantitative measurement was started to be carried out. The existence of β^+ decay even with a very small branching ratio $(3.186\pm0.047)\times10^{-5}$ (Selwyn, Nickles, Thomadsen, DeWerd, & Micka, 2007) leads to internal pair production interaction between β^+ and the β^-, thus producing two annihilation photons with the same energy (~511 keV) in the opposite direction. This process is the basis of PET imaging (Saha, 2016).

The discussion below elaborates general technical issues of SPECT and PET in the use of ^{90}Y biodistribution measurement, it highlights the active use of each, and reminds the possible remaining challenges to be improved in both systems.

2.2 Spect

Several investigations had been carried out to evaluate SPECT-based post-radioembolization measurement which is still facing many problems (Elschot M, 2011; L. M. Minarik D, Segars P, Gleisner KS, 2009; S.-G. K. Minarik D, Linden O, Wingardh K, Tennvall J, et al, 2010). Since the indirect bremsstrahlung x rays is a continuous spectrum which lacks photopeaks (Elschot M, 2011), the discrimination of counts based on the energy of the photon becomes difficult. As an effort to improve the SPECT sensitivity, a large energy window is required (Elschot M, 2011), which at the same time, allows for more noise caused by background radiation and scatter photons (Cherry, Sorenson, & Phelps, 2012). The resulted contrast also get reduced with the use of collimator septa, a mechanical aperture made of lead. The collimator septa are needed for locating the counting events, but at the same time, its existence also allows for high energy photon penetration and thus degrades the image quality (Elschot M, 2011). All those factors that eventually influence the overall performance characteristics of SPECT are examined in detail in the next section.

Some studies tried to improve the image quality of SPECT by concerning the following ways. The first is to find the optimal energy windows, either using Monte Carlo (MC) simulation of the full energy spectrum (Heard, 2004; Rault, Staelens, Holen, Beenhouwer, & Vandenberghe, 2010) or phantom studies (Minarik, Gleisner, & Ljungberg, 2008). Second, by modeling of the image degrading factor, which can be done by employing the simulation of imaging nuclear detector (SIMIND) (Rong, Du, Ljungberg, et al., 2012) or again, the MC simulation-based modeling (Elschot, Lam, Bosch, Viergever, & Jong, 2013). Based on the studies previous studies, it

can be figured out that the optimal energy windows for detection of ^{90}Y are in the middle energy range of approximately 100-150 keV, 100-160 keV, or 90-125 keV, respectively (Heard, 2004; Rong, Du, & Frey, 2012; Shen S, 1994). The lower energy range (70-100 keV) is mainly resulted by characteristics photon coming from the lead collimator, while the higher energy range (200-300 keV) and >300 keV mostly comes from backscattering and septal penetration, respectively (Heard, 2004). The latter approach by modeling of degrading factors yields a significantly better image contrast, from 25% to 88% for the 37 mm sphere and less count error detection from 73% to 15%, accompanied by the increase of noise (Mattijs Elschot et al., 2013).

Though the SPECT system suffers from poor sensitivity and spatial resolution, there are some counter facts, which in turn makes SPECT is advantageous in some cases (Bailey & Willowson, 2013). As the SPECT radionuclides have longer half-lives, there is no urgency of placing a medical cyclotron near the SPECT facility. A simultaneous multi-tracer study is also possible when it is needed to assess two or more radionuclide biokinetics in a single session. Lastly, the SPECT system requires less investment as compared to PET and has the greater use worldwide.

2.3 PET

The current practice of post-radioembolization ^{90}Y SIRT imaging was firstly initiated by Nickles et al. in 2004 by using phantom studies (Nickles et al., 2004), while the clinical study was firstly performed by Lhommel et al. in 2009 (Lhommel et al., 2009). Later, a PET-based dosimetry was confirmed to be feasible with the additional Time of Flight (TOF) (Lhommel et al., 2010) or even without the TOF installation (Werner et al., 2009). Indeed, the utilization of TOF is likely producing a better estimation of dose as investigated by several groups (Attarwala et al., 2014; Carlier et al., 2015; Elmbt, Vandenberghe, Walrand, Pauwels, & Jamar, 2011; Martí-Climent et al., 2014; Willowson, Forwood, Jakoby, Smith, & Bailey, 2012; Willowson, Tapner, & Bailey, 2015). It is because the use of TOF improves the sensitivity and spatial resolution due to its ability to provide high coincidence time resolution and accurate coincidence location detection (Walrand, Hesse, Renaud, & Jamar, 2015). The TOF design itself has been much developed for the last three decades, where the coincidence time resolution gets reduced from 650 ps in the first prototype, down to 320 ps in the latest digital TOF-PET, each providing the annihilation location prediction within 9 cm and 4.5 cm, respectively (Surti & Karp, 2016). The improvement of TOF-PET system nowadays is the result of the utilization of lutetium-based crystal (Lutetium oxy-orthosilicate, LSO, and lutetium–yttrium oxy-orthosilicate, LYSO), which is better than bismuth germinate (BGO) crystal in term of faster decay time and higher photon to light conversion output (Surti & Karp, 2016).

There are several promising facts to support the capability of PET in the use of ^{90}Y imaging. First, as the annihilation photons have approximately uniform energy (~511 keV), the discrimination window may easier to distinguish the true coincidence, despite the possibility of scattering, random, and multiple coincidences, and thus producing better sensitivity and spatial resolution. Second, the maximum positron energy of ^{90}Y is 758 keV that is comparable to the 633 keV of ^{18}F (Bailey DL, 2003). Consequently, the correction techniques including scatter, random, and attenuation correction are expected to be clinically suitable for the well-established correction procedure for ^{18}F (van Elmbt L, 2010).

As a functional imaging tool, it is well understood that PET also suffers from several limitations which degrade the accuracy of its measurement (IAEA, 2014). Naturally, the positrons travel a certain distance (~4 mm) before the annihilation events occur (Cherry et al., 2012). It inevitably produces an uncertainty in events location detection. The other issue is the probability of block effect or depth of interaction (J., 2013). In this phenomena, the interaction of annihilation photon does not only take place in the corresponding two detectors but also penetrate in the neighboring detectors which end up in the wrong line of response (LOR) (J., 2013). Furthermore, there is also a possible non-collinearity detection between the two annihilation photons direction. This effect

may significantly affect the resolution for the larger ring diameter (Cherry et al., 2012). The other case is that the spatial resolution is not uniform for the whole field of view (FOV). Instead, the highest resolution is achieved in the middle of FOV and getting worse towards the periphery (Cherry et al., 2012). As the spatial resolution is characterized by point spread function (PSF), there is a so-called PSF algorithm included in the image reconstruction process to improve the spatial resolution (Rahmim, Qi, & Sossi, 2013).

IMAGE QUALITY IN QUANTITATIVE IMAGING

Description of image quality in quantitative imaging can usually be made based on several aspects, including spatial resolution, contrast, noise, and detectability (M. Elschot et al., 2013). Representative images of SPECT and PET are illustrated in Fig. 2. In general, PET images can provide a better representation of the lesion shape and higher activity uptake as compared to SPECT images (Y.-H. Kao et al., 2013).

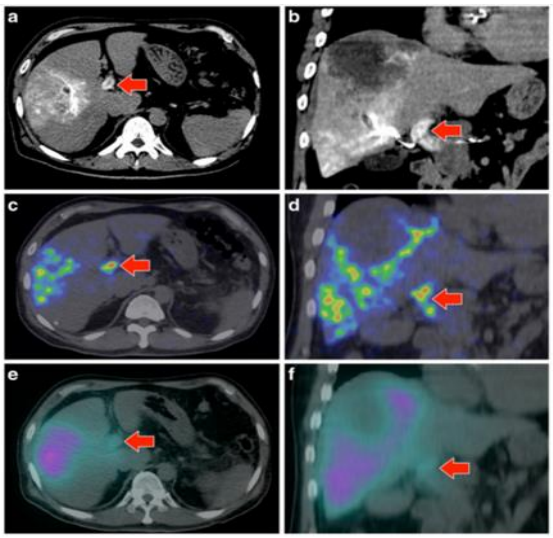

Fig 2. Large heterogeneous liver lesions shown in three different modalities. (a, b) Catheter-directed CT angiogram (c, d) 90Y PET/CT (e, f) 90Y bremsstrahlung SPECT/CT. This picture was reproduced from Kao et al., 2013.

3. RESULTS AND DISCUSSION

3.1 Spatial Resolution

The spatial resolution is defined as the ability to distinguish two adjacent points and characterized by the full width half maximum (FWHM). An insufficient spatial resolution produces the blurring and also lead to partial volume effect which may reduce quantitative accuracy (Soret, Bacharach, & Buvat, 2007). Investigation of image resolution performed based on 90Y SPECT yields the range of 11.4 – 12.5 mm (for a source to detector distance of 6 – 6.5 mm) (Elschot M, 2011; Shen S, 1994). Meanwhile, the image resolution of PET laid between 2.2 – 12.1 mm (Attarwala et al., 2014; Carlier et al., 2015; Elmbt et al., 2011; Martí-Climent et al., 2014; Willowson et al., 2012; Willowson et al., 2015), respectively. However, this value may differ between each type of device, the type of microsphere used, the type of scintillator crystal, and the reconstruction parameter as shown in Table III. Nevertheless, in general, the spatial resolution of PET is still superior relatively compared to SPECT.

Contrast and Noise

Elschot et al. compared the contrast and noise in the two imaging modalities (Mattijs Elschot et al., 2013). The contrast recovery and noise are the parameters of interest because it affects the distinction of the lesion object and the adjacent background. They employed several methods to assess the influence of PSF algorithm and the additional TOF to the resulted images. For all methods, the iterative reconstruction was set. The results are shown in Fig. 3 and Fig. 4.

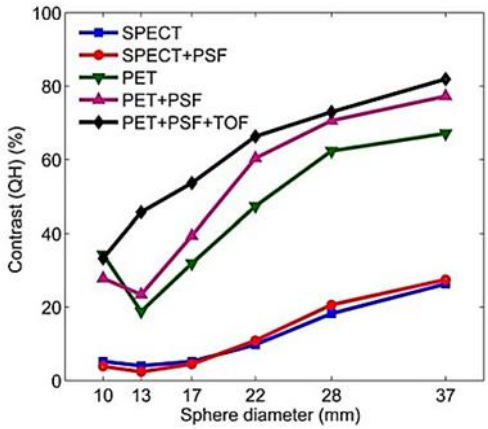

Fig 3. Contrast recovery as a function of sphere diameter for all reconstruction methods used in SPECT and PET. This picture was taken from Elschot, et al., 2013.

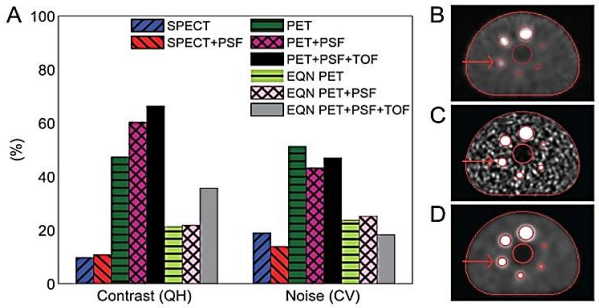

Fig 4. SPECT and PET contrast recovery and image noise. A. Contrast recovery and image noise in the 22-mm sphere for all reconstruction methods, B. SPECT image (iterative+PSF), C. PET (iterative+PSF+TOF), D. PET (iterative+PSF+TOF) reconstructed with SPECT-like noise level.

The picture was taken from Elschot et al., 2013.

According to Fig. 3, the overall images showed that the contrast recovery was higher for the PET image, where the highest contrast was achieved by the iterative+PSF+TOF and followed by the iterative+PSF method. In contrary, the use of PSF algorithm did not give any difference to the contrast recovery of SPECT. In line with the contrast recovery parameter, noise levels are also significantly higher in the PET images where the incorporation of PSF algorithm and TOF notably reduced the noise level. Ideally, it is desired to have a sufficient contrast with less noise presence. Therefore, the post-reconstruction processing was performed and obtained the PET image (iterative+PSF+TOF) with the SPECT-like noise level to establish better contrast and noise composition.

3.2 Detectability

The detectability comparison between SPECT and PET was demonstrated according to two criteria, i.e. Rose criterion for false negative detection and the method described by Elschot et al. (Mattijs Elschot et al., 2013) to analyze the detectability in the intra- and extrahepatic biodistribution accumulation simulated in a phantom. Though the Rose criterion results indicate that all sites in the intra- and extrahepatic are visible, the other method denoted different outcomes. While the extrahepatic site remained visible up to as small as 28 mm in the diameter in PET image, all spheres in SPECT did not. In the intrahepatic site, the detectability thresholds are 13 and 22 mm for PET and SPECT, respectively. After all, this analysis signifies the superiority of the PET over SPECT in detecting the intra- and extrahepatic arteries.

PERFORMANCE CHARACTERISTICS

The excellence of quantitative imaging system can also be evaluated based on their performance characteristics. There are several measures, including spatial resolution, sensitivity, recovery coefficient, image uniformity, count rate linearity, calibration factor, and convergence of the image reconstruction algorithm (Cherry et al., 2012; J., 2013). This review will cover the comparison of SPECT and PET characteristics in term of spatial resolution and sensitivity.

3.3 SPECT Characteristics

Elschot et al. characterized the spatial measurement and sensitivity of SPECT and listed in Table I-II. In their research, a material called polymethylmethacrylate or PMMA was placed in the position between the source and detector to create the realistic condition of electron scattering. The data were taken based on several different object-to-source distances, namely, 2, 6, and 11 cm was set for 1 cm of scattering material, and 11 cm for 5 and 10 cm of scattering material. Two kinds of windows were used, which consisted of a broad (50-250 keV) and a smaller (120-250 keV) energy windows. There were also two types of collimator used, medium-energy (MEGP) and high-energy-multi-purpose (HEGP) collimators (Elschot M, 2011). The spatial resolution and sensitivity were then determined according to NEMA guideline (Association, 2007), where the sensitivity was obtained by the ratio of acquired counts and the true activity measured in a dose calibrator. The sensitivity was calculated for two positions, 10 cm and 40 cm from the detector (Elschot M, 2011).

In Table I, the number on the outside and inside the bracket showed the FWHM and FWTM, respectively. The spatial resolution is substantially better when the source-detector-distance is kept remained close. Also, the use of smaller energy window (120-250 keV) and the HEGP collimator notably produced preferable

spatial resolution (smaller FWHM) (Elschot M, 2011). The result in this study was in line with another publication by Shen et al., in which they obtained FWHM of 12.5 mm measured at 6.8 mm source-object-distance in the energy window of 55-285 keV (Shen S, 1994). Meanwhile, the nearest setting in the Elschot et al.'s work provided FWHM of 11.4 mm (Elschot M, 2011).

Table 1. Spatial resolution of SPECT-based ^{90}Y imaging

	^{90}Y 120-250 keV		**90Y 50-250 keV**	
	MEGP	**HEGP**	**MEGP**	**HEGP**
S01D02	11.5(173.7)	7.0(113.1)	10.9(123,2)	7.5(49.2)
S01D06	12.9(222.2)	11.0(137.2)	11.4(149.7)	11.1(60.2)
S01D11	17.1(286.1)	15.3(160.0)	15.8(172.9)	15.4(57.6)
S05D11	19.7(300.6)	16.4(218.9)	19.4(235.7)	17.0(159.3)
S10D11	28.1(341.2)	18.1(269.5)	26.3(294.9)	20.1(241.3)

The spatial resolution is written in mm unit.

S01D02 corresponds to the measurement with 1 cm of scatter material and line-source to collimator distance of 2 cm, S01D06 to the measurement with 1 cm of scatter material and line-source to collimator distance of 6 cm, etc.

This table was reproduced based on Elschot, et al., 2011.

The sensitivity obtained here was also consistent with another publication where they obtained 11.6 and 6.75 cps MBq^{-1} for MEGP and HEGP, in the broad energy window (Shen S, 1994). As may be expected, the broad energy window yielded higher sensitivity as consequence of involvement of scattering fraction and background counts. For the same energy window, the MEGP collimator produced higher sensitivity than the HEGP (Elschot M, 2011; Shen S, 1994).

Table 2. Sensitivity of SPECT-based ^{90}Y Imaging

	^{90}Y 120-250 keV		^{90}Y 50-250 keV	
	MEGP	HEGP	MEGP	HEGP
S – 10 cm (cps MBq^{-1})	6.0	3.1	10.5	6.0
S – 40 cm (cps MBq^{-1})	3.0	1.8	6	4.9

This table was reproduced based on Elschot, et al., 2011.

3.4 PET Characteristics

Many authors have recently reported investigations on PET spatial resolution with different modification factors as summarized in Table III. The assessment of spatial resolution in PET is commonly performed by using NEMA guideline NU 2-2007 (Association, 2007). The choice of the scintillation crystal, the utilization of TOF, reconstruction parameter seemed to be a matter of the final spatial resolution results. As stated before, the LSO is a good material for the PET detector design (Surti & Karp, 2016). Accompanied by a high number of iteration and subsets, though without TOF, the resolution of 90Y PET imaging can reach 2.5 to 4 mm resolution (Gates, Esmail, Marshall, Spies, & Salem, 2010).

The sensitivity determination also takes into account the true activity from dose calibrator measurement. Later, the counts reported in the PET system is divided by the true activity to obtain the sensitivity value, the same calculation performed in SPECT. Some factors are influencing the determination of sensitivity, such as detection efficiency, source-detector geometrical position, and acquisition mode (2D, with septa, or 3D, without septa). The detection efficiency concerns on conversion from photon to light, and is affected by some parameters, including scintillation decay time, atomic number, density, and the thickness of the scintillation material (Cherry et al., 2012).

The sensitivity of ^{90}Y PET was measured by several authors (Bagni et al., 2012; Ng et al., 2013; Werner et al., 2009). The absolute sensitivity measured using Biograph mCT-TrueV with TOF was 0.403 and 0.388 cps MBq^{-1} in the center of FOV and 10 cm of the FOV, respectively (Martí-Climent et al., 2014). Another work by Bagni et al. performed by using GE Discovery ST PET/CT provided similar results, which are 0.409 and 0.577 cps MBq^{-1} for the same position setting (Bagni et al., 2012). In comparison with the well-known ^{18}F, the sensitivity of ^{90}Y is much smaller, about four order below the sensitivity of ^{18}F ($\approx$0.5 versus 9 cps MBq^{-1}) (D'Arienzo et al., 2012). It can be

explained by the fact that the positron abundance of ^{90}Y is only 32 per one million decays, whereas the ^{18}F gains almost 967 per 1000 decays (Pasciak et al., 2017).

Table 3. Spatial Resolution of PET-based 90Y Imaging as the results of different acquisition and reconstruction methods

Reference	^{90}Y MICROSPHERE	Scanner manufacturer	Detector crystal	Acquisition mode	Reconstruction	Resolution
Lhommel et al. (2010) (Lhommel et al., 2010)	Resin microsphere	Gemini Phillips	LYSO	TOF	2 iterations, 33 substeps	-
Werner et al. (2010) (Werner et al., 2009)	Resin Microspheres	Biograph Hi-Rez Siemens	LSO	Non TOF	8 iterations 16 subsets and 4 iterations 8 subsets	6.4 mm
Gates et al (2011) (Gates et al., 2010)	Glass microspheres	Biograph 40 Siemens	LSO	Non TOF	3 iteration, 21 subsets	2.5 – 4 mm
Wissmeyer et al. (2011) (Wissmeyer et al., 2011)	Glass microspheres	Philips Gemini PET/MR	LYSO	TOF	3 iterations, 33 subsets	-
Bagni et al. (2011) (Bagni et al., 2012)	Resin microspheres	Discovery ST GE	BGO	Non TOF	2 iterations, 15 subsets	6.3 mm
Carlier et al. (2013) (Carlier et al., 2015)	Resin microspheres	Biograph mCT 40 Siemens	LSO	TOF and Non TOF	1 or 3 iterations, 21 or 24 subsets	-
Elschot et al. (2013) (Mattijs Elschot et al., 2013)	Resin microspheres	Biograph mCT Siemens	LSO	TOF	3 iterations, 21 or 24 subsets	-
Kao et al. (2012) (Y. e. a. Kao, 2012)	Resin microspheres	Biograph WO Siemens	LSO	Non TOF	2 iterations, 8 subsets	-
Kao et al. (2013) (Mattijs Elschot et al., 2013)	Resin microspheres	Discovery 690 GE	LYSO	TOF	3 iterations, 18 subsets	10 – 12 mm
van Elmbt et al. (2011) (Elmbt et al., 2011)	Resin microspheres	Philips Gemini TF	LYSO	TOF	3 iterations, 8 subsets	9.3 mm
van Elmbt et al. (2011) (Elmbt et al., 2011)	Resin microspheres	Philips Gemini Power16	GSO	Non TOF	3 iterations, 8 subsets	10 mm
van Elmbt et al. (2011) (Elmbt et al., 2011)	Resin microspheres	Siemens Ecat Exact HRb	BGO	Non TOF	3 iterations, 8 subsets	10.6 mm
Martí-Climent et al. (2014) (Martí-Climent et al., 2014)	Resin microspheres	Biograph mCT-TrueV	LSO	TOF	1–3 iterations, 21–24 subsets	2.2 – 12.1 mm

This table was reproduced based on Pasciak AS, et al., 2017.

Indonesian Journal of Physics and Nuclear Applications
Volume 4, Number 2, June 2019, p. 45-57
e-ISSN 2550-0570, © FSM UKSW Publication

ABSORBED DOSE CONSIDERATION

Image-based quantitative dosimetry was performed for both SPECT (iterative+PSF) and PET (iterative+PSF+TOF) images in both phantom and patient studies (M. Elschot et al., 2013). For phantom dosimetry, due to the small size of ROIs, they encountered PVE, and thus, a corrected dose was also estimated. The results were compared to the true value which was determined based on high-resolution CT data. The results were shown in Fig. 5-6 and Table IV-V. Among all cumulative dose volume histograms (CDVHs) in the phantom study, the PET sphere CDVH appeared to be the closest to the true CDVH. The PET sphere CDVH was a bit differ to the true sphere CDVH in the form of the flat curve because it was influenced by the substantially higher noise in the PET image. Also, the overall dose measured based on PET (corrected and uncorrected dose) consistently showed the least difference to the true value. For instance, the smallest diameter measured by SPECT and PET achieved -75% (+69%) and -45% (+40%) dose difference to the true value, respectively. As the PVE did not strongly affect large diameter, the dose difference tends to be lower, which are -58% (+18%) and -11% (+6%) for SPECT and PET, respectively. Analog to CDVH results, the patient dosimetry showed more significant dose difference between the low dose (LD) and high dose (HD) in the PET-based dose estimation. For example, the dose difference in the SPECT-dose map (Fig. 5B) and PET-dose map (Fig. 5C) are 39 and 73 Gy. It was also supported by the substantial gap between the PET HD and SPECT HD CDVHs curves. According to this result, it was concluded that the high-resolution PET with the TOF installation and PSF reconstruction algorithm likely produced a better image of ^{90}Y distribution in post-radioembolization imaging.

Table 4. Phantom Dosimetry

	Phantom ROI (mm)						
	10	13	17	22	28	37	Background
SPECT	76 (516)	69 (514)	78 (511)	102 (487)	143 (484)	181 (508)	61
PET	167 (431)	224 (432)	255 (433)	333 (475)	324 (426)	384 (457)	60
TRUE	306	341	372	395	412	432	52

This table was repreoduced based on Elschot, et al.,2013.

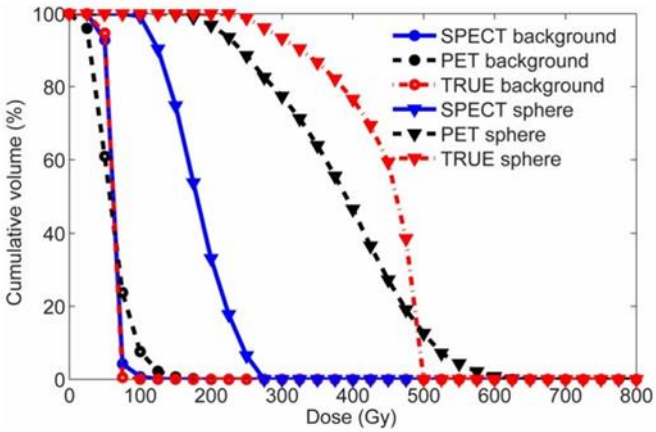

Fig 5. Phantom dosimetry. CDVH of the phantom background ROI and the ROI of the 37-mm diameter sphere. The presented doses were not corrected for PVE. The figure was taken from Elschot, et al., 2013.

Table 5. Patients dosimetry

	Phantom ROI (mm)									
	1		2		3		4		5	
	LD	HD	LD	HD	LD	HD	LD	HD	LD	HD
SPECT	26	37	34	73	30	53	22	36	12	31
PET	29	85	38	111	33	80	26	58	11	47

The mean dose (Gy) in the low-dose ROI (LD) and the high-dose ROI (HD) are given for all patients. This table was repreoduced based on Elschot, et al., 2013.

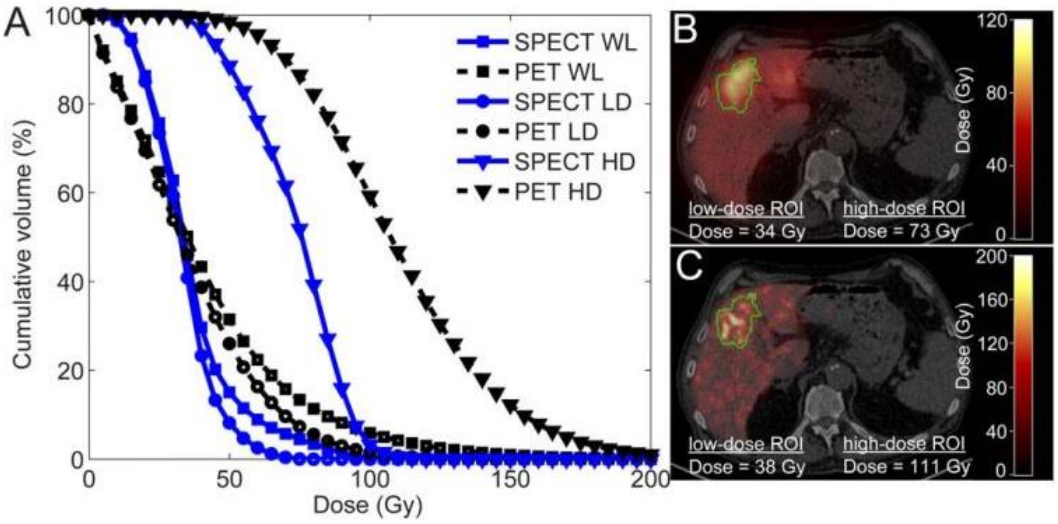

Fig 6. Patient dosimetry. The CDVH of the whole liver (WL), low-dose (LD) and high-dose (HD) ROIs of patient 2 (A), a transversal slice through the SPECT-based dose map, fused with CT (B), and the same transversal slice through the PET-based dose map (C). The boundary of the high dose ROI is depicted by the green line. The figure was taken from Elschot, et al., 2013.

4. CONCLUSION AND REMARKS

The emerging use of ^{90}Y Radioembolization SIRT needs a reliable post-treatment imaging modality because of its function to produce a quantitative image as the basis of dose estimation and dose-response analyses. In term of image quality, considering the spatial resolution, noise, contrast, and detectability, the high-resolution PET-based image well demonstrates these parameters relatively compared to the SPECT-based image. The high-resolution PET may be achieved by the installation of TOF, the use of the iterative algorithm with a high number of subsets and iterations, the use of PSF algorithm, and the utilization of lutetium-based scintillation crystal. In contrast to the large underestimation or overestimation of dose in SPECT-based dosimetry, the PET dosimetry seemed to be closer to the true value. When the high-resolution PET is used, the dose estimation still needs to consider the correction of PVE which may exist for the small lesion site.

REFERENCES

Association, N. E. M. (2007). NEMA NU 2-2007 Performance. In *Measurements of Positron Emission Tomographs* Aelington, VA: NEMA.

Attarwala, A. A., Molina-Duran, F., Büsing, K.-A., Schönberg, S. O., Bailey, D. L., Willowson, K., & Glatting, G. (2014). Quantitative and qualitative assessment of yttrium-90 PET/CT imaging. *PLoS One, 9*, e110401.

Bagni, O., D'Arienzo, M., Chiaramida, P., Chiacchiararelli, L., Cannas, P., D'Agostini, A., . . . Scopinaro, F. (2012). 90Y-PET for the assessment of microsphere biodistribution after selective internal radiotherapy. *Nucl Med Commun, 33*(198-204).

Bailey DL, K. J., Surti S (2003). Physics and instrumentation in PET. In T. D. Bailey DL, Maisey MN. (Ed.), *Positron Emission Tomography: Basic Science and Clinical Practice.* (pp. 41–67). London: Springer-Verlag.

Bailey, D. L., & Willowson, K. P. (2013). An evidence-based review of quantitative SPECT imaging and potential clinical applications. *The Journal of Nuclear Medicine, 54*(1), 83-90.

Bé, M.-M., et al. (2006). *Table of radionuclides*. Sèvres, Paris: Bureau International des Poids et Mesures.

Biermann HR, B. R., Kelley KH, Grady A. (1951). Studies on the blood supply of tumors in man. III. Vascular patterns of the liver by hepatic

arteriography in vivo. *J Natl Cancer Institute, 12*.

Carlier, T., Willowson, K. P., Fourkal, E., Bailey, D. L., Doss, M., & Conti, M. (2015). 90Y-PET imaging: Exploring limitations and accuracy under conditions of low counts and high random fraction. . *Med Phys, 42*, 4295–4309.

Cherry, S. R., Sorenson, J. A., & Phelps, M. E. (2012). *Physics in Nuclear Medicine*. Philadelphia, PA: Elsevier/Saunders.

D'Arienzo, M., Chiaramida, P., Chiacchiararelli, L., Coniglio, A., Cianni, R., Salvatori, R., . . . Bagni, O. (2012). 90Y PET-based dosimetry after selective internal radiotherapy treatments. *Nucl Med Commun, 33*, 633–640.

Doherty, J. O. (2015). A review of 3D image-based dosimetry, technical considerations and emerging perspectives in 90Y microsphere therapy. *J Diagn Imaging Ther, 2*(2), 1-34. doi::10.17229/jdit.2015-0428-016.

Elmbt, L. v., Vandenberghe, S., Walrand, S., Pauwels, S., & Jamar, F. (2011). Comparison of yttrium-90 quantitative imaging by TOF and non-TOF PET in a phantom of liver selective internal radiotherapy. *Phys Med Biol, 56*, 6759–6777.

Elschot, M., Lam, M. G. E. H., Bosch, M. A. A. J. v. d., Viergever, M. A., & Jong, H. W. A. M. d. (2013). Quantitative Monte Carlo–based 90Y SPECT reconstruction. *J Nucl Med, 54*, 1557–1563.

Elschot M, N. J., Dam AJ, de Jong HW. (2011). Quantitative evaluation of scintillation camera imaging characteristics of isotopes used in liver radioembolization. *PLoS One, 6*, e26174.

Elschot, M., Vermolen, B. J., Lam, M. G., de Keizer, B., van den Bosch, M. A., & de Jong, H. W. (2013). Quantitative comparison of PET and Bremsstrahlung SPECT for imaging the in vivo yttrium-90 microsphere distribution after liver radioembolization. *PLoS One, 8*(2), e55742. doi:10.1371/journal.pone.0055742

Ford, K. (1955). Predicted 0+ level of Zr90. *Phys Rev, 98*, 1516–1517.

Gates, V. L., Esmail, A. A. H., Marshall, K., Spies, S., & Salem, R. (2010). Internal pair production of 90Y permits hepatic localization of microspheres using routine PET: Proof of concept. *J Nucl Med, 52*, 72–76.

Giammarile, F., Bodei, L., Chiesa, C., Flux, G., Forrer, F., Kraeber-Bodere, F., . . . Luster, M. (2011). EANM procedure guideline for the treatment of liver cancer and liver metastases with intra-arterial radioactive compounds. *Eur J Nucl Med Mol Imaging*. doi:DOI 10.1007/s00259-011-1812-2

Gulec, S. A., Mesoloras, G., & Stabin, M. (2006). Dosimetric Techniques in 90Y-Microsphere Therapy of Liver Cancer: The MIRD Equations for Dose Calculations. *J Nucl Med., 11*, 1209.

Heard, S., Flux, G.D., Guy, M.J., Ott, R.J. (2004). Monte Carlo simulation of 90Y bremsstrahlung imaging. *IEEE Nucl Sci Symp Conf Record, 6*, 3579–3583.

Ho S, L. W., Leung TWT, Chan M, Johnson PJ, Li AKC. (1997). Clinical evaluation of the partition model for estimating radiation doses from yttrium-90 microspheres in the treatment of hepatic cancer. *Eur J Nucl Med Mol Imaging, 24*, 293–298.

IAEA. (2014). *IAEA Human Reports No. 9: Quantitative Nuclear Medicine Imaging: Concepts, Requirements and Methods*. Retrieved from Viena:

J., P. (2013). *Nuclear Medicine Instrumentation.* Boston London Toronto Singapore: Jones and Bartlett Publishers.

Johnson O, J. R., Langer L. (1955). Evidence for a 0+ frst excited state in Zr90. *Phys Rev, 98*, 1517–1518.

Kao, Y.-H., Steinberg, J. D., Tay, Y.-S., Lim, G. K., Yan, J., Townsend, D. W., . . . Goh, A. S. (2013). Post-radioembolization yttrium-90 PET/CT – part 1: diagnostic reporting. *EJNMMI Research, 3*(56), 1-13.

Kao, Y. e. a. (2012). Yttrium-90 internal pair production imaging using frst generation PET/CT provides high-resolution images for qualitative diagnostic purposes. . *Br J Radiol, 85*, 1018–1019.

Kao YH, T. E., Ng CE, Goh SW. (2011). Clinical implications of the body surface area method versus partition model dosimetry for yttrium-90 radioembolization using resin microspheres: a technical review. *Ann Nucl Med., 25*, 455–461. doi:10.1007/s12149-011-0499-6

Lau, W. Y., Kennedy, A. S., Kim, Y. H., Lai, H. K., Lee, R. C., Leung, T. W., . . . Wang, S. C. (2012). Patient selection and activity planning guide for selective internal radiotherapy with yttrium-90 resin microspheres. *Int J Radiat Oncol Biol Phys, 82*(1), 401-407. doi:10.1016/j.ijrobp.2010.08.015

Leung TW, L. W., Ho SKW, Ward SC, Chow JHS, Chan MSY, et al. (1995). Radiation pneumonitis after selective internal radiation treatment with intraarterial 90Yttrium-

microspheres for inoperable hepatic tumors. *Int J Radiat Oncol Biol Phys. , 33*, 919–924.

Lhommel, R., Elmbt, L. v., Goffette, P., Eynde, M. V. d., Jamar, F., Pauwels, S., & Walrand, S. (2010). Feasibility of 90YTOF PET-based dosimetry in liver metastasis therapy using SIR-spheres. *Eur J Nucl Med Mol Imaging, 37*, 1654–1662.

Lhommel, R., Goffette, P., Eynde, M. V. d., Jamar, F., Pauwels, S., Bilbao, J. I., & Walrand, S. (2009). Yttrium-90 TOF PET scan demonstrates high-resolution biodistribution after liver SIRT. *Eur J Nucl Med Mol Imaging, 36*, 1696–1696.

Martí-Climent, J. M., Prieto, E., Elosúa, C., Rodríguez-Fraile, M., Domínguez-Prado, I., Vigil, C., . . . Richter, J. A. (2014). PET optimization for improved assessment and accurate quantifcation of 90Y-microsphere biodistribution after radioembolization. *Med Phys, 41*, 092503.

Minarik, D., Gleisner, K. S., & Ljungberg, M. (2008). Evaluation of quantitative 90Y SPECT based on experimental phantom studies. *Phys Med Biol, 53*, 5689–5703.

Minarik D, L. M., Segars P, Gleisner KS. (2009). Evaluation of quantitative planar 90Y bremsstrahlung whole-body imaging. *Phys Med Biol, 54*, 5873–5883.

Minarik D, S.-G. K., Linden O, Wingardh K, Tennvall J, et al. (2010). 90Y Bremsstrahlung imaging for absorbed-dose assessment in high-dose radioimmunotherapy. *J Nucl Med, 51*, 1974–1978.

Murthy, R., Brown, D. B., Salem, R., Meranze, S. G., Coldwell, D. M., Krishnan, S., . . . Censullo, M. (2007). Gastrointestinal complications associated with hepatic arterial yttrium-90 microsphere therapy. *J Vasc Interv Radiol, 18*, 553–562.

Murthy, R., Nunez, R., Szlklaruk, J., Erwin, W., Madoff, D. C., Gupta, S., . . . Hicks, M. E. (2005). Yttrium-90 microsphere therapy for hepatic malignancy: devices, indications, technical considerations, and potential complications. *Radiographics, 25*, 41-55.

Ng, S. C., Lee, V. H., Law, M. W., Liu, R. K., Ma, V. W., Tso, W. K., & Leung, T. W. (2013). Patient dosimetry for 90Y selective internal radiation treatment based on 90Y PET imaging. *J Appl Clin Med Phys, 14*, 212–221.

Nickles, R. J., Roberts, A. D., Nye, J. A., Converse, A. K., Barnhart, T. E., Avila-Rodriguez, M. A., . . . Thomadsen, B. R. (2004). Assaying and PET imaging of yttrium-90: 1>>34 ppm>0. *IEEE Nucl Sci Symp Rec 6:3412–3414., 6*, 3412–3414.

Pasciak, A. S., Bradley, Y., & McKinney, J. M. (2017). *Handbook of Radioembolization*. Florida: CRC Press Taylor & Francis

Rahmim, A., Qi, J., & Sossi, V. (2013). Resolution modeling in PET imaging: Theory, practice, benefits, and pitfalls. *Med. Phys., 40*(6), 064301-064301 - 064315.

Rault, E., Staelens, S., Holen, R. V., Beenhouwer, J. D., & Vandenberghe, S. (2010). Fast simulation of yttrium-90 bremsstrahlung photons with GATE. *Med Phys, 37*, 2943–2950.

Riaz, A., Lewandowski, R. J., Kulik, L. M., Mulcahy, M. F., Sato, K. T., Ryu, R. K., . . . Salem, R. (2009). Complications Following Radioembolization with Yttrium-90 Microspheres: A Comprehensive Literature Review. *J Vasc Interv Radiol, 20*, 1121–1130.

Rong, X., Du, Y., & Frey, E. C. (2012). A method for energy window optimization for quantitative tasks that includes the effects of model-mismatch on bias: Application to Y-90 bremsstrahlung SPECT imaging. *Phys Med Biol, 57*(12), 3711–3725.

Rong, X., Du, Y., Ljungberg, M., Rault, E., Vandenberghe, S., & Frey, E. C. (2012). Development and evaluation of an improved quantitative 90Y bremsstrahlung SPECT method. *Med Phys, 39*, 2346–2358.

Saha, G. B. (2016). *Basics of PET Imaging: Physics, Chemistry, and Regulations* (Vol. 3). Cham Heidelberg New York Dordrecht London: Springer.

Selwyn, R. G., Nickles, R. J., Thomadsen, B. R., DeWerd, L. A., & Micka, J. A. (2007). A new internal pair production branching ratio of 90Y: the development of a non-destructive assay for 90Y and 90Sr. *Appl Radiat Isot, 65*(3), 318-327. doi:10.1016/j.apradiso.2006.08.009

Shen S, D. G., DeNardo SJ. (1994). Quantitative bremsstrahlung imaging of yttrium-90 using a Wiener flter. *Med Phys, 21*(9), 1409-1417.

Soret, M., Bacharach, S. L., & Buvat, I. (2007). Partial-volume effect in PET tumor imaging. *J Nucl Med, 48*(6), 932-945. doi:10.2967/jnumed.106.035774

Stabin, M. G. (2006). Nuclear medicine dosimetry. *Phys Med Biol., 51*, R187–202. doi:10.1088/0031-9155/

Stabin, M. G. (2008). Uncertainties in internal dose calculations for radiopharmaceuticals. Journal of Nuclear Medicine. *J Nucl Med, 49*(5), 853-860.

Stubbs, R. S., & Wickremesekera, S. K. (2004). Selective internal radiation therapy (SIRT): a

new modality for treating patients with colorectal liver metastases. *HPB (Oxford), 6*(3), 133-139. doi:10.1080/13651820410025084

Surti, S., & Karp, J. S. (2016). Advances in time-of-flight PET. *Phys Med, 32*(1), 12-22. doi:10.1016/j.ejmp.2015.12.007

van Elmbt L, W. S., Lhommel R, Jamar F, Pauwels S. (2010). Quantitative comparison between LYSO and BGO PET-tomographs in 90Y imaging. *Eur J Nucl Med Mol Imaging, 37*, S293–S293.

Walrand, S., Hesse, M., Renaud, L., & Jamar, F. (2015). The impact of image reconstruction bias on PET/CT 90Y dosimetry after radioembolization. *J Nucl Med, 56*, 494–495.

Werner, M. K., Brechtel, K., Beyer, T., Dittmann, H., Pfannenberg, C., & Kupferschläger, J. (2009). PET/CT for the assessment and quantifcation of 90Y biodistribution after selective internal radiotherapy (SIRT) of liver metastases. . *Eur J Nucl Med Mol Imaging, 37*, 407–408.

Willowson, K., Forwood, N., Jakoby, B. W., Smith, A. M., & Bailey, D. L. (2012). Quantitative 90Y image reconstruction in PET. *Med Phys, 39*, 7153.

Willowson, K., Tapner, M., & Bailey, D. L. (2015). A multicentre comparison of quantitative 90Y PET/CT for dosimetric purposes after radioembolization with resin microspheres. *Eur J Nucl Med Mol Imaging, 42*, 1202–1222.

Wissmeyer, M., Heinzer, S., Majno, P., Buchegger, F., Zaidi, H., Garibotto, V., . . . Terraz, S. (2011). 90Y time-of-flight PET/MR on a hybrid scanner following liver radioembolisation (SIRT). *Eur J Nucl Med Mol Imaging, 38*, 1744–1745.